Acta Acustica united with Acustica
Vol. 103 (2017) 954 – 966

DOI 10.3813/AAA.919125

Application of the Factorisation Method to Limited Aperture Ultrasonic Phased Array Data

Katherine M. M. Tant[1)], Anthony J. Mulholland[1)], Anthony Gachagan[2)]
[1)] Department of Mathematics and Statistics, University of Strathclyde, Glasgow, UK. katy.tant@strath.ac.uk
[2)] Centre for Ultrasonic Engineering, University of Strathclyde, Glasgow, UK

Summary
This paper puts forward a methodology for applying the frequency domain Factorisation Method to time domain experimental data arising from ultrasonic phased array inspections in a limited aperture setting. Application to both synthetic and experimental data is undertaken and a multi-frequency approach is explored to address the difficulty encountered in empirically choosing the optimum frequency at which to operate. Additionally, a truncated singular value decomposition (TSVD) approach is implemented in the case where the flaw is embedded in a highly scattering medium, to regularise the scattering matrix and minimise the contribution of microstructural noise to the final image. It is shown that when the Factorisation Method is applied to multi-frequency scattering matrices, it can better characterise crack-like scatterers than in the case where the data arises from a single frequency. Finally, a volumetric defect and a lack-of-fusion crack are both successfully reconstructed from experimental data, where the resulting images exhibit only 3% and 10% errors respectively in their measurement.

PACS no. 43.35.-c, 43.35.Zc

1. Introduction

Ultrasonic nondestructive testing uses high frequency mechanical waves to inspect components of safety critical structures, ensuring that they operate reliably without compromising their integrity. It is routinely used within the non-destructive testing (NDT) industry due to the relatively inexpensive and portable equipment it requires and its potential for automation and real-time results. The production and implementation of ultrasonic phased array transducers (which are capable of simultaneously transmitting and receiving ultrasound signals across multiple array elements) has surged in the last ten years [1]. These multi-element transducers allow for greater coverage (and potentially faster inspection times) than that afforded by single probe inspections, and provide the possibility of performing inspections with ultrasonic beams at various angles and focal lengths, giving rise to a richer set of data. When each of the N elements are fired sequentially, the N^2 time traces arising from each transmit-receive pair of elements (N being the number of elements, usually between 32 and 256) can be processed and stored in a 3D matrix ($N \times N \times T$, where T is the number of sample points in the time domain), usually termed the Full Matrix Capture (FMC) [2].

Received 23 February 2017,
accepted 7 August 2017.

The current industry benchmark for interpreting the FMC is the Total Focussing Method (TFM) [2]; a delay and sum imaging technique based in the time domain where the area of inspection is discretised into a grid and the signals from every transmit-receive pair are subsequently focussed at each pixel and su mmed. In its most basic form, the TFM can struggle with the detection and characterisation of flaws embedded in highly heterogeneous media. However, efforts have been made to improve the algorithm so that it can handle such environments. Modifications include the implementation of frequency filtering [3], the incorporation of the directional dependence of the ultrasonic velocity (caused by anisotropy) [4], and the consideration of multiple wave modes [5].

An alternative approach to analysing the FMC could be to operate in the frequency domain. Assuming that the location of the flaw is known *a priori*, a discrete Fourier transform can be taken over the relevant time interval, allowing examination of the frequency spectrum of the wave scattered by the flaw. This information can be presented in the form of scattering matrices, and analysis of these matrices has become more prevalent in the non-destructive testing literature in recent years [6, 7, 8, 9]. One method which could be used to exploit this frequency domain information is the Factorisation Method [10, 11, 12, 13]. The Factorisation Method is the continuous analogue of the MUSIC algorithm [14, 15] and belongs to a class of non-iterative methods known as sampling methods, which deal with the inverse problem of shape identifi-

cation. Other such methods include the Linear Sampling Method [16, 17], the Probe Method [17, 18] and the Singular Sources Method [17, 19]. These sampling methods are so named since they work on the basis of determining whether sampled points within an imaging domain meet some criteria which determines whether they fall within the support of the flaw domain D.

The NDT community have yet to fully explore the potential of the Factorisation Method for improved flaw characterisation and this paper endeavours to put forward a framework for applying it to time domain experimental data arising from limited aperture phased array inspections. Some interesting work has already been carried out in [13, 20], where sampling methods were used to image cracks in acoustic waveguides, which of course has important implications for the NDT of pipelines. However this work showed only results from simulated data with Gaussian noise and is limited to the inspection of plate-like structures. One important contribution of the work shown in this paper is that it presents a framework for interrogating time domain ultrasonic phased array data arising from the inspection of welds, by the Factorisation Method. Application of sampling methods to time domain data has been studied before in [20, 21, 22, 23, 24] however the authors believe that this paper presents application of the Factorisation Method to experimentally collected time domain ultrasonic phased array data in a limited aperture setting for the first time. The case where the host medium is inhomogeneous (resulting in poor signal to noise ratio) is first considered via synthetically generated data. The phased array inspection of a weld with a highly scattering material microstructure (taken from experimental electron backscatter diffraction (EBSD) measurements) is modelled within a finite element package. This allows us to study noisy signals which closer resemble the data arising from experiment than those created when the simulation is run with a homogeneous host medium and then retrospectively perturbed by random noise. Note that the implementation of the factorisation methodology used in this paper assumes a homogeneous host medium and receives no information on the scattering host microstructure and so any inverse crimes are avoided. The reconstructions of both volumetric and crack-like scatterers embedded in this heterogeneous environment are presented. Crack-specific adaptations to the Factorisation method and the linear sampling method have been developed in [13, 25, 26, 27]. In the study by Boukari *et al.* [27], an expression for the far-field pattern of a smooth non intersecting open arc is presented and employed within the indicator function used to reconstruct the scatterer. However, in [25], an open arc scatterer with Dirichlet boundary conditions is reconstructed using the far-field pattern for a point source. In this paper, on the grounds of simplicity, we will take the second approach. To begin, a brief overview of the method is given. The truncated singular value decomposition (TSVD) is used to regularise the scattering matrices that arise from the FMC data in the cases where the flaw is embedded in a highly scattering host medium. It is well known that the largest scatterers can be associated with the largest eigenvalues of the scattering matrix [28] and so, by using the TSVD to set the smallest eigenvalues to zero, interference from microstructural heterogenetites (which can be thought of as noise) can be reduced, enhancing the signal to noise ratio of the resulting image.

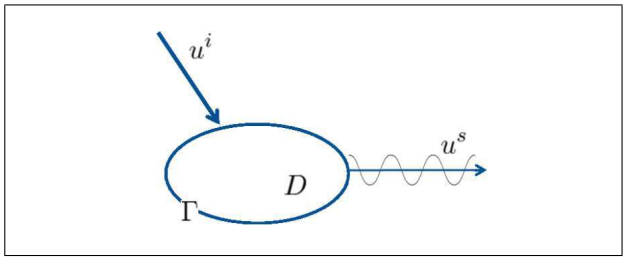

Figure 1. Scattering problem geometry where D is a volumetric scatterer with boundary Γ, u^i is the incident plane wave and u^s is the resulting scattered field.

Additionally, a multi-frequency approach, as previously explored in [29], is adopted. In taking a time windowed Fourier transform of collected time domain data, a range of scattering matrices spanning multiple frequencies is made available. Choosing the center frequency of the transducer does not necessarily give rise to the optimal reconstruction of the flaw and an empirical strategy to choose the most appropriate frequency requires *a priori* knowledge of the defect's characteristics. To avoid this, a multi-frequency approach is proposed, where the scattering matrices are summed over the range of frequencies which span the bandwidth of the transducer. As this approach allows increased exploitation of the available data, improved characterisation is subsequently facilitated.

2. The Factorisation Method

The forward scattering problem states that there is an incident plane wave, $u^i(x,\theta) = \mathrm{e}^{\mathrm{i}kx\cdot\theta}, x \in \mathbb{R}$, travelling in direction $\theta \in S^2$, where $S^2 = \{x \in \mathbb{R}^3 : |x| = 1\}$ is the unit sphere in $\mathbb{R}^3$. On encountering a defect, in this case the region D with boundary Γ, the wave scatters, giving rise to the scattered field u^s (see Figure 1). The sum of the incident and scattered fields results in the total field u, which satisfies the Helmholtz equation

$$\begin{aligned} \Delta u + k^2 u &= 0 \quad \text{outside } D, \\ \text{subject to} \quad u &= 0 \quad \text{on } \Gamma, \end{aligned} \tag{1}$$

where k is the wavenumber. Although we are primarily interested in the elastodynamic case for the purposes of NDT, by considering only longitudinal waves (mode conversion does occur however the method we use to extract the scattering matrices is based on first times of arrival and so is dominated by the longitudinal waves – see Section 3) then it is sufficient to study the Helmholtz equation. The scattered field u^s satisfies the Sommerfeld radiation condition

$$\frac{\partial u^s}{\partial r} - \mathrm{i}ku^s = \mathcal{O}(r^{-1}) \quad \text{for} \quad r = |x| \to \infty \tag{2}$$

uniformly in all directions $\hat{x} = x/|x|$, ensuring that the wave is radiating outwards and decays sufficiently fast so that there are no sources at infinity.

The scattered field u^s also solves the exterior Dirichlet problem

$$\begin{aligned} &\Delta v + k^2 v = 0 \quad \text{outside } D, \\ &\text{subject to} \quad v = f \quad \text{on } \Gamma, \end{aligned} \tag{3}$$

where $f = -u^i$ and v satisfies the Sommerfeld radiation condition given in (2).

The Factorisation Method [10, 11, 12] attempts to solve the inverse problem of determining the shape of D from the scattered field. The methodology exploits the relationship between the data-to-pattern operator G and the shape of the scatterer. To begin with, let u^{sph} be the fundamental, radiating solution to the Helmholtz equation in $\mathbb{R}^3$ (a spherical wave generated at a point source z and measured at point x, in a homogeneous host medium) given by

$$u^{sph}(x, z) = \frac{\mathrm{e}^{\mathrm{i}k|x-z|}}{4\pi|x-z|}, \quad x, z \in \mathbb{R}^3, \quad x \neq z. \tag{4}$$

As the distance between x and z gets large (far-field), the spherical wave begins to resemble a plane wave at point x. This can be approximated by

$$u^{\infty}(\hat{x}) = \mathrm{e}^{-\mathrm{i}k\hat{x}\cdot z}, \quad \hat{x} \in S^2, \tag{5}$$

where u^{∞} is the far-field pattern when we have an incident wave arising from a point source.

The Herglotz wave function describes the superposition of plane waves

$$\big(Hg\big)(x) := \int_{S_2} \mathrm{e}^{\mathrm{i}kx\cdot\theta} g(\theta)\, \mathrm{d}\theta, \quad x \in \Gamma, \tag{6}$$

with density $g \in L^2(S^2)$. The far-field pattern arising from an incident plane wave applied to some function g is the far-field pattern of the Herglotz wave function with density g. By denoting the far-field pattern of the scattered field (obtained from our measured data), by u_s^{∞}, we can define the far-field operator F by

$$Fg(\hat{x}) = \int_{S^2} u_s^{\infty}(\hat{x}, \theta) g(\theta)\, \mathrm{d}s(\theta) \quad \text{for } \hat{x} \in S^2. \tag{7}$$

Note that F is a normal operator and compact in $L^2(S^2)$. Deriving the following factorisation of the operator F [10, Theorem 1.15],

$$F = -GP^*G^*, \tag{8}$$

is the basis for the Factorisation Method. Here $P^* : H^{-1/2}(\Gamma) \to H^{1/2}(\Gamma)$ is the L^2 adjoint of the single layer boundary operator $P : H^{-1/2}(\Gamma) \to H^{1/2}(\Gamma)$

$$P\varphi(x) = \int_{\Gamma} u^{sph}(x, y)\varphi(y)\, \mathrm{d}s(y), \quad x \in \Gamma. \tag{9}$$

and effectively converts the incoming wave to an outgoing wave on the defect boundary. The operator $G^* : L^2(S^2) \to H^{-1/2}(\Gamma)$ is the L^2 adjoint of $G : H^{1/2}(\Gamma) \to L^2(S^2)$, the data-to-pattern operator, defined by

$$Gf = u^{\infty}. \tag{10}$$

Critically, the range $\mathcal{R}(G)$ of the operator G has a direct relationship to the shape of the domain D. For $z \in \mathbb{R}^3$, $\phi_z \in L^2(S^2)$ is defined by

$$\phi_z(\hat{x}) = \mathrm{e}^{-\mathrm{i}k\hat{x}\cdot z}, \quad \hat{x} \in S^2. \tag{11}$$

It follows that if $z \in D$, then, from equations (5) and (11), $\phi_z = u^{\infty}$ and so, from equation (10), $\phi_z \in \mathcal{R}(G)$ when $z \in D$.

The converse is also true according to Theorem 1.12 in [10]. To gain an exact characterisation of $\mathcal{R}(G)$ in terms of the known operator F, we can relate G to F by equation (8). To proceed, some further technical assumptions are required. It is assumed that F, for the Dirichlet boundary conditions (Equation 1), is normal, the operator $I + ikF/8\pi^2$ is unitary and k^2 is not a Dirichlet eigenvalue of $-\Delta$ in D (these conditions are justified in [10]). It then holds that the range of $(F^*F)^{1/4}$ coincides with that of G. Hence, the sampling point $z \in \mathbb{R}^3$ lies in D if and only if

$$\big(F^*F\big)^{1/4} g = \phi_z \tag{12}$$

for some $g \in L^2(S^2)$.

By Picard's criterion, equation (12) is solvable if and only if the condition $\phi_z \in \mathcal{R}((F^*F)^{1/4})$ is satisfied (this is shown to hold by equations (5)–(10)). It then follows that, $z \in D$ if and only if

$$\sum_{j=1}^{\infty} \frac{|(\phi_z, \psi_j)_{L^2(S^2)}|^2}{|\lambda_j|} < \infty, \tag{13}$$

where $\{\lambda_j, \psi_j\}$ forms an eigensystem of the normal operator F such that the eigenvectors define a complete orthonormal system in $L^2(S^2)$ and the Fourier coefficients decay to zero faster than the eigenvalues. Using the spectral theory of a normal operator, [10, equation 1.74] it is observed

$$(F^*F)^{-1/4}\phi_z = \sum_{j=1}^{\infty} \frac{1}{\sqrt{|\lambda_j|}} (\phi_z, \psi_j)\psi_j \tag{14}$$

$$\iff \sum_{j=1}^{\infty} \left| \frac{1}{\sqrt{|\lambda_j|}} (\phi_z, \psi_j) \right|^2 < \infty, \tag{15}$$

and so equation (13) does indeed hold. From equations (12) and (14), the solution g is given by

$$g = \sum_j \frac{\big(\phi_z, \psi_j\big)_{L^2(S^2)}}{\sqrt{|\lambda_j|}} \psi_j, \tag{16}$$

and the following result is obtained

$$\begin{aligned} z \in D &\iff \phi_z \in \mathcal{R}((F^*F)^{1/4}) \\ &\iff W(z) = \left[\sum_j \frac{|(\phi_z, \psi_j)_{L^2(S^2)}|^2}{|\lambda_j|} \right]^{-1} > 0. \end{aligned} \tag{17}$$

In practice, we use the $N \times N$ scattering matrix in place of our operator F (where N is the number of array elements). Assuming F is normal (and thus diagonalizable), it holds that there exist N linearly independent eigenvectors. Thus, when using this discrete, limited aperture, we truncate equation (17) to

$$w(z) = \left[\sum_{j=1}^{N} \frac{|(\phi_z, \psi_j)_{L^2(S^2)}|^2}{|\lambda_j|} \right]^{-1} > \varepsilon, \quad z \in D, \quad (18)$$

where $\varepsilon > 0$. By plotting $w(z)$ for all sampling points, z, it is possible to recover the shape and size of the defect.

2.1. The $F_\#$ Operator

It was shown above that a sampling point z lies within the domain D of the scatterer if and only if there exists a solution in $L^2(S^2)$ to equation (12). However, this criterion only holds if the far-field operator F is normal, which is not always the case when limited angles of inspection or heterogeneous host materials are present. To circumvent this, the positive, self-adjoint operator $F_\#$ is introduced [10, 30] where

$$F_\# = |Re(F)| + |Im(F)|, \quad (19)$$

and

$$Re(F) = \frac{1}{2}(F + F^*) \quad \text{and} \quad Im(F) = \frac{1}{2i}(F - F^*). \quad (20)$$

It is helpful to note here that for a given self-adjoint operator J, if

$$J = \int_{-\infty}^{+\infty} \lambda \, \mathrm{d}E_\lambda, \quad (21)$$

then

$$\mathrm{d}\left|J\right| := \int_{-\infty}^{+\infty} \left|\lambda\right| \mathrm{d}E_\lambda, \quad (22)$$

where E_λ is the spectral family of the operator J [13]. As F is compact in $L^2(S^2)$ it follows that F^* is compact in $L^2(S^2)$ and thus so is $F_\#$ [31]. It can be subsequently shown that a sample point z belongs to the domain D if and only if the integral equation

$$F_\#^{1/2} g = \phi_z \quad (23)$$

has a solution in $L^2(S^2)$ [10] (here ϕ_z is as defined in equation (11)). It follows that, by plotting

$$W(z) = \left[\sum_{j=1}^{N} \frac{|(\phi_z, \psi_j^\#)_{L^2(S^2)}|^2}{|\lambda_j^\#|} \right]^{-1}, \quad z \in \mathbb{R}^2, \quad (24)$$

where $\{\lambda_j^\#, \psi_j^\#\}_{j \in \mathbb{N}}$ forms an eigensystem of the self-adjoint operator $F_\#$ such that the eigenvectors define a complete orthonormal system in $L^2(S^2)$, an image of the scatterer can be reconstructed.

2.2. Truncated SVD of the Scattering Matrix

From equation (24), we can see that $W(z)$ is large when ϕ_z is orthogonal to the eigenvectors of $F_\#$, which occurs when the sampling point lies within the spatial domain occupied by the flaw. The other occasion when $W(z)$ could be large is when $\lambda_j^\#$ is large for some $j = 1, \ldots, N$, even when $z \notin D$ and so $(\phi_z, \psi_j^\#)_{L^2(S^2)} \neq 0$.

To minimise the contribution of these cases, an artificial nullspace is created. This is achieved by taking the singular value decomposition (SVD) of the $N \times N$ scattering matrix, F^*, and approximating it using the m largest singular values via

$$F^* = \sum_{n=1}^{m} \sigma_n u_n v_n, \quad (25)$$

thus creating a nullspace with dimension $N - m$. In the case of subwavelength non-isotropic scatterers, the largest eigenvalue is associated with the spherically sy mmetric part of the scattering amplitude and there are three eigenvalues associated with the directional part [32, 33]. Where the scatterer is larger than the wavelength, there exist many singular values associated with it. And so, in the work below we make the constraint that $m \geq 4$. Aside from this lower bound, we typically assume that the singular values which are greater than 10% of the largest singular value correspond to scattering by the defect and those below this threshold correspond to noise and scattering by the microstructure [15, 34]. However, by studying the distributions of the singular values it can be observed that this threshold may not always be optimal and may require some tuning subject to the system parameters.

3. Application to NDT

The results in this paper arise from application of the Factorisation Method to data collected (or modelled) in the time domain. To interrogate the data using the Factorisation Method, we require a frequency domain representation of the scattered signals over a time interval corresponding to the wave's interaction with the flaw. To ensure that the flaw scattering dominates in the frequency domain and that other experimental artifacts (such as the back wall of the sample) don't obscure the flaw's scattering signature, the time domain FMC data must be processed. Firstly the location of the flaw is required *a priori* (it must be remembered that the Factorisation Method is being applied here as a post-imaging tool for flaw characterisation). In this paper, the defect is located using an image generated by the standard TFM [2]

$$I(x, z) = \left| \sum_{s,r=1}^{N} A_{s,r} \left(\frac{\sqrt{(x_s - x)^2 + z^2} + \sqrt{(x_r - x)^2 + z^2}}{c} \right) \right|, \quad (26)$$

where $I(x, z)$ is the image intensity at the pixel with coordinates (x, z), $A_{s,r}$ denotes the A-scan (that is, the time

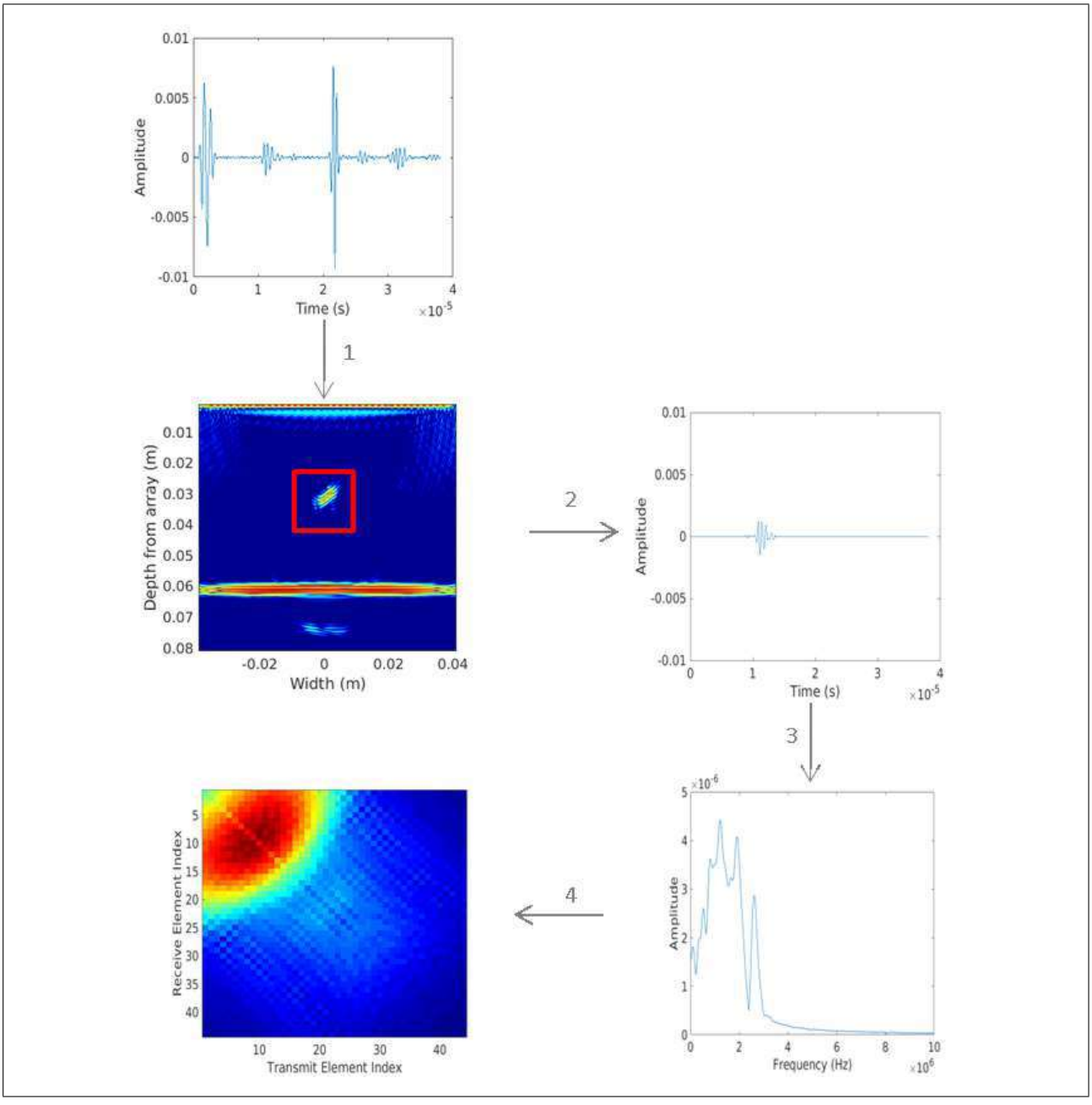

Figure 2. Processing of time domain FMC data for extraction of scattering matrices. Firstly the flaw is located using the standard TFM. Then, the distance of the defect from the array coupled with the estimated wave speed gives rise to a time interval pertaining to scattering by the defect. The Fourier transform is applied to the FMC data in this interval. Then, the amplitude at a specified frequency is plotted for each transmit-receive pair to generate the scattering matrix.

series data) when a wave is emitted at location x_s and received at location x_r and c is the estimated constant wave speed throughout the host medium. When the distance of the defect from the array is known, it can be coupled with the estimated wave speed c to give rise to a time pertaining to scattering by the defect. Some interval is taken around this value and a discrete Fourier transform is applied. From the resulting spectral data a scattering matrix can be generated at a chosen frequency by plotting the amplitude of the power spectrum at that frequency for every transmit-rece ive pair. The scattering matrix is then assigned as the operator F and the Factorisation Method can be applied accordingly. This process is depicted in Figure 2 and can be summarised in four key steps:

1. Apply the TFM algorithm (see equation (26)) to the raw FMC data to find the location of the defect.
2. For each pair of transmit-receive elements, calculate the distance from the transmitter x_s to the centre of the defect in the TFM image and back to the receiver x_r. Coupled with the wavespeed in the material, c, calculate the point of interest in time, $t_{s,r}$. Take an interval centered round $t_{s,r}$ on each set of time series data $A_{s,r}$.
3. Take a discrete Fourier transform over this interval to obtain the frequency spectrum $Y_{s,r}$.

4. The amplitude of $Y_{s,r}$ at a specific frequency f is assigned as the element $F_{s,r}$ of the scattering matrix F at that frequency.

Note that the size of the time interval depends on the size of the defect and its proximity to other scatterers (we would ideally not incorporate data arising from other scatterers within the interval). It is clear that, for every FMC dataset there exists a set of scattering matrices, each one at a different frequency. Choosing a frequency at which to operate is not straightforward: the best reconstructions rarely arise from the scattering matrix generated at the center frequency of the transducer. Identifying which single frequency results in the optimal reconstruction of the flaw requires *a priori* knowledge of the defect dimensions. Hence, a multi-frequency approach (where scattering matrices spanning at least the −6 dB bandwidth of the transducer are summed at regular intervals) is introduced, exploiting more of the information made available by the bandwidth of the transducer whilst removing the subjective aspect of identifying the frequency which affords the best flaw reconstruction.

3.1. Simulated and Experimental Data Sets

In this paper, the Factorisation Method is applied to data arising from two sources. Firstly, the scattering of an ultrasonic wave by a flaw is simulated using a time domain finite element method in the software package PZFlex [35]. In this paper, three FMC datasets generated using this method are examined (the parameters are listed in Tables I and II). Firstly the scattering by a 5 mm crack with 40° orientation (relative to the horizontal axis) embedded in a homogeneous medium was simulated. The same flaw was then placed in a heterogeneous environment where the locally anisotropic microstructure of an austenitic steel weld (derived from experimental electron backscatter diffraction measurements [36]) was embedded in the simulation (see Figure 3). In both instances the domain was meshed with elements of dimension $\lambda/15$, where lambda is the wavelength. The 1.5 MHz sinusoidal excitation used thus gave rise to elements approximately 200 µm square, which is sufficient to accurately model the wave propagation. In the heterogeneous case, the weld structure consisted of grains where contigious crystallites with similar orientations were grouped together to form locally anisotropic regions. The correlation length [37] was estimated as $\lambda/8$ and the RMS longitudinal velocity through this heterogeneous medium was estimated as 5758 m/s with a standard deviation of 146 m/s (calculated using the times corresponding to the backwall echo in the A-scans where transmission and reception took place on the same element). The location of the flaw and this estimated average wave speed were then used to isolate the time interval pertaining to the flaw and the relevant scattering matrices were thus obtained (see Section 3 and Figure 2). Note that by isolating the time interval using the estimated longitudinal velocity, shear wave scattering (which should occur at a later time) is neglected, as is secondary scattering which occurs after the wave has reflected off the back wall and interacts with the defect on its return journey. The third simulated dataset examines an alternative scenario where a 2.5 mm side-drilled hole is embedded in the parent stainless steel material to the left of the weld microstructure, at a depth of 30 mm from the array (this is similar to the experimental sample as detailed in Table III). A schematic is shown in Figure 4, with parameters recorded in Table II. The RMS longitudinal velocity through this sample medium was estimated as 5801 m/s with a standard deviation of 363 m/s (relatively large as approximately N/2 elements lay over the homogeneous parent material and the others over the anisotropic weld structure).

Table I. Parameters used in the FE simulation of an ultrasonic phased array inspection of an embedded 5 mm crack. H.M.: Homogeneous Medium, M.I.: Microstructure Included.

	H.M.	M. I.
Number of Array Elements	64	64
Pitch	2 mm	2 mm
Transducer Center Frequency	1.5 MHz	1.5 MHz
Depth of Flaw	50 mm	50 mm
Depth of Sample	78.4 mm	78.4 mm
Material Density	7874 kg/m^3	7874 kg/m^3
Estimated wave speed (from TFM)	5900 m/s	5758 m/s

Table II. Parameters used in the FE simulation of an ultrasonic phased array inspection of an 2.5 mm diameter side-drilled hole.

	Value	Unit
Number of Array Elements	128	-
Pitch	0.7	mm
Transducer Center Frequency	2.25	MHz
Sample Rate	25	MHz
Depth of Sample	50	mm
Depth of Flaw from Array	30	mm
Flaw diameter	2.5	mm
Estimated wave speed	5801	m/s

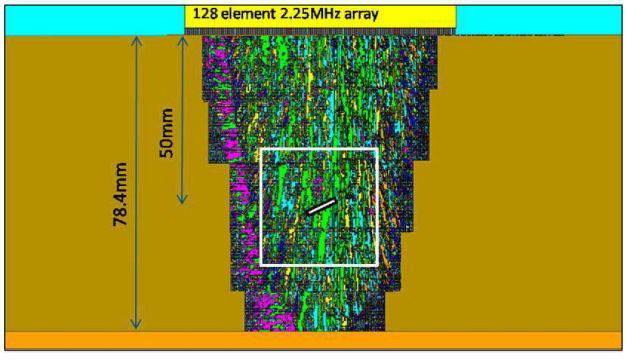

Figure 3. Geometry input to the finite element simulation where a 5 mm crack with 40° orientation (relative to the horizontal axis) is embedded in an austenitic weld microstructure. The 128 element 2.25 MHz array is placed directly above the flaw over the weld material. The white box depicts the sampling domain.

Table III. System parameters for the experimental phased array inspection of a 3 mm diameter side-drilled-hole embedded next to an ultrasonically noisy MMA weld.

	Value	Unit
Number of Array Elements	128	-
Pitch	0.7	mm
Transducer Center Frequency	2.25	MHz
Sample Rate	25	MHz
Depth of Sample	50	mm
Depth of Flaw from Array	30	mm
Flaw diameter	3	mm
Estimated wave speed	5580	m/s

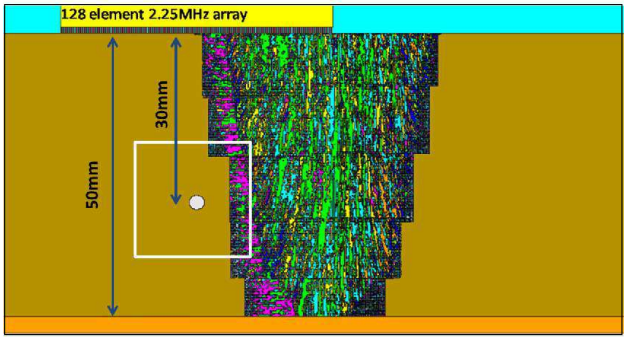

Figure 4. Geometry input to the finite element simulation where a 2.5 mm diameter side-drilled hole is embedded in the parent material (stainless steel) close to a highly scattering polycrystalline region which represents an austenitic steel weld. The 128 element 2.25 MHz array is placed directly above the flaw over the parent and weld materials. The white box depicts the sampling domain.

Secondly, the Factorisation Method was applied to experimental data. The first test sample considered in this paper is a steel block containing an ultrasonically noisy manual metal arc (MMA) weld. The defect of interest is a 3 mm diameter side drilled hole lying to the left of the weld, 30 mm from the front face of the 50 mm thick sample, as shown in Figure 5. The inspection was carried out by a 2.25 MHz linear array (Vermon, France) as specified in Table III combined with the Zetec DYNARAY® (Zetec, Canada) array controller. The RMS longitudinal velocity through this heterogeneous medium was estimated as 5580m/s with a standard deviation of 192 m/s. Note that these values differ from the comparable simulation described in Table II as the weld geometry used in the simulation does not come from this particular sample and provides only an estimate of the effects of multiple scattering in the ultrasonically noisy MMA weld present in the experiment. TFM images were constructed using this experimentally derived phase velocity to identify the location of the defect before scattering matrices were generated as discussed in Section 3.

The second experimental test sample considered was manufactured from welded austenitic steel plates with implanted defects. The defect of interest is a 7.8 mm lack-of-fusion crack between the weld and steel plate, lying at a 50° angle, relative to the horizontal axis, in close proximity to the back surface of the sample (see Figure 6). The inspection was carried out by a 5 MHz linear array (Vermon, France) as specified in Table IV, combined with the Zetec DYNARAY® (Zetec, Canada) array controller. The RMS longitudinal velocity through this heterogeneous medium was estimated as 5820 m/s. As before, relevant time intervals were isolated using TFM imaging and scattering matrices were thus generated.

Table IV. System parameters for the experimental phased array inspection of a 7.8 mm lack-of-fusion crack on the boundary of an austenitic double V weld.

	Value	Unit
Number of Array Elements	128	-
Pitch	0.7	mm
Transducer Center Frequency	5	MHz
Sample Rate	100	MHz
Depth of Sample	22	mm
Depth of Flaw from Array	16	mm
Estimated wave speed	5820	m/s

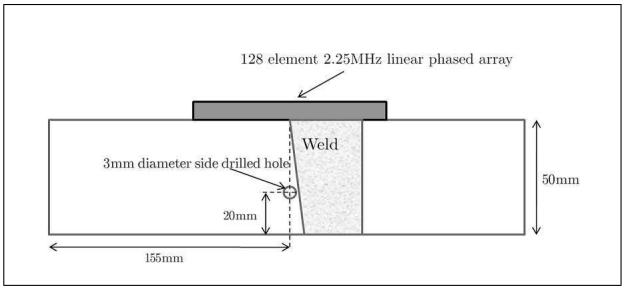

Figure 5. This schematic depicts a cross section (the x-z plane in which we are interested) of a steel sample containing an ultrasonically noisy MMA weld. A 3 mm diameter flaw is embedded in the parent material to the left of the the weld (marked by the hatched area) and the 128 element 2.25 MHz array is placed centrally above the defect, over the parent and weld materials.

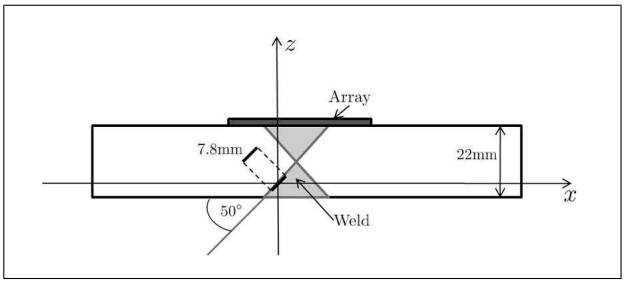

Figure 6. This schematic depicts a cross section (the x-z plane in which we are interested) of the stainless steel test sample constructed from welded austenitic plates of 22 mm depth. A lack-of-fusion crack of 7.8 mm length lies along the left hand side of the weld (marked by the shaded area) at an angle of 50° (relative to the horizontal axis).

3.2. Application to FMC Data Generated by the Finite Element Method

In [10] it is indicated that in the case of limited aperture data, where the far-field pattern $u^\infty(\hat{x}, \theta)$ is known only for $\hat{x}, \theta \in U, U \subset S^2$ (that is, where there is a limited angle of inspection), the far-field operator F is not normal. As the FMC data used in this paper arises from ultrasonic inspections by a linear phased array, the Factorisation Method is applied to the $F_\#$ operator here (see Section 2.1).

Figure 7 depicts reconstructions of a 5 mm crack orientated at 40° to the horizontal axis, embedded in a homogeneous medium, using FMC data generated by the time domain finite element method (see Section 3.1, Table I). Note that the sampling domain is a 20 mm^2 region centered on the flaw (see Figures 3 and 4) and this remains constant for all reconstructions shown in this paper. As discussed in Section 3, only a subset of the FMC dataset (arising from the central 44 elements) has been considered in order to exclude scattering by the backwall. This offers an angular aperture of only 83°, less than one quarter of the full aperture (360°) at which the Factorisation Method performs optimally. No TSVD has been taken here as the flaw is embedded in a completely homogeneous medium and the null space of the scattering matrix already exists. The image is plotted over a 6 dB dynamic range (a standard threshold for measuring defects larger than one wavelength) where the outermost contour is aligned to this limit. Figure 7a shows the known geometry and size of the defect. Image (b) depicts the reconstruction generated by applying the Factorisation Method to the single frequency (1.5 MHz) scattering matrix. Although the resulting image is oversized (11.7 mm in length) and includes two lower amplitude artefacts, the method has identified the defect as a tilted ellipse-like scatterer. As discussed in Section 3, it is possible that improved reconstructions of the flaw may be achieved at different frequencies. However, without *a priori* knowledge of the flaw's dimensions, the optimal frequency cannot be deduced. Thus the multi-frequency approach was adopted to generate image (c) where scattering matrices were generated over the range 0.75 MHz–2.25 MHz, at intervals equal to the sampling frequency f_s, and then summed. Again, the result is a tilted ellipse although this time the additional artifacts have disappeared and an improved crack length estimate of 9.6 mm is achieved.

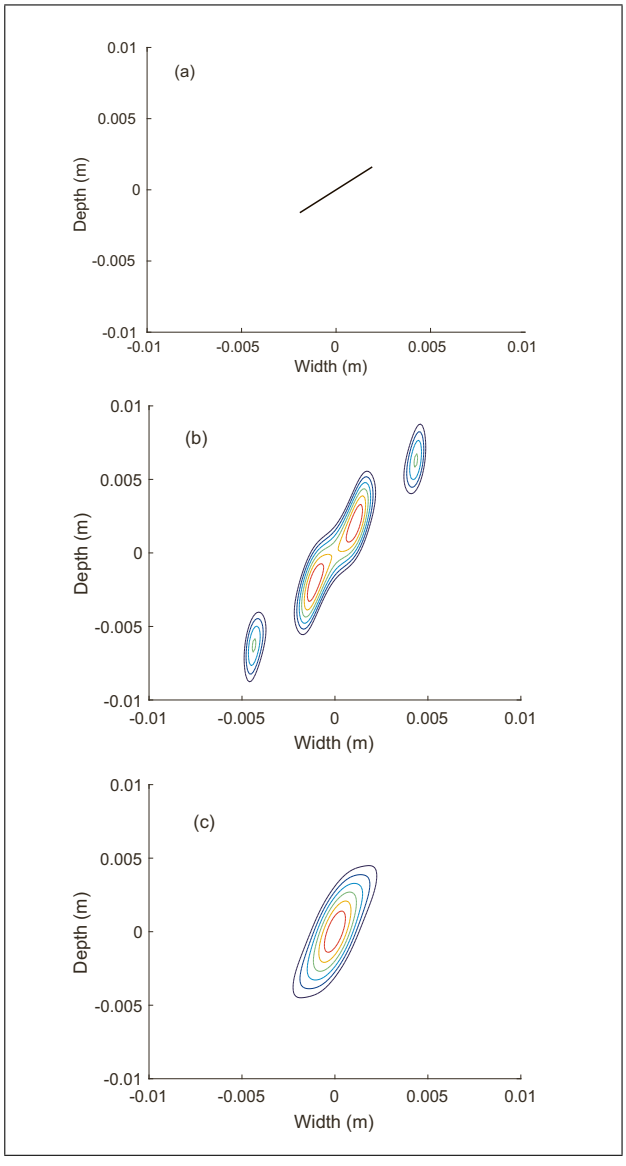

Figure 7. Crack reconstructions from FMC data arising from finite element simulation of the scattering of ultrasonic waves by a 5 mm crack with 40° orientation embedded in a homogeneous medium. Image (a) depicts the known defect size and geometry. This was reconstructed by (b) the Factorisation Method applied to the scattering matrix arising at 1.5 MHz and (c) the Factorisation Method applied to the multi-frequency scattering matrix.

To further assess the suitability of the Factorisation Method for application in NDT, it has been applied to data arising from the FEM simulation of an ultrasonic wave scattered by a 5 mm crack of 40° orientation (relative to the horizontal axis) embedded in a heterogeneous medium (see Section 3.1 for details and Figure 7a for the defect size and geometry). Again, to exclude the signals where the flaw scattering is conflated with that of the back wall, only the data arising from the central 44 array elements is considered (an angular aperture of only 83°). In Figure 8, results from application of the Factorisation Method to variants of the scattering matrix are plotted. Image (a) shows the reconstruction arising from the single frequency (1.5 MHz), non regularised ($m = 44$) scattering matrix, measuring 7.3 mm. Image (b), demonstrates the result when only the first four largest singular values are used to approximate a smoother single frequency scattering matrix at 1.5 MHz ($m = 4$). Although the measurement is 9 mm, the method has correctly determined that we are dealing with a crack-like flaw. Image (c) arises from the multi-frequency (spanning the range 0.75 MHz-2.25 MHz at intervals of f_s), non-regularised ($m = 44$) scattering matrix, and the 6dB contour measures 5.03 mm across. Unfortunately, the fact that the crack is tilted is almost entirely lost in this reconstruction. When the multi-frequency approach is combined with the TSVD ($m = 4$),

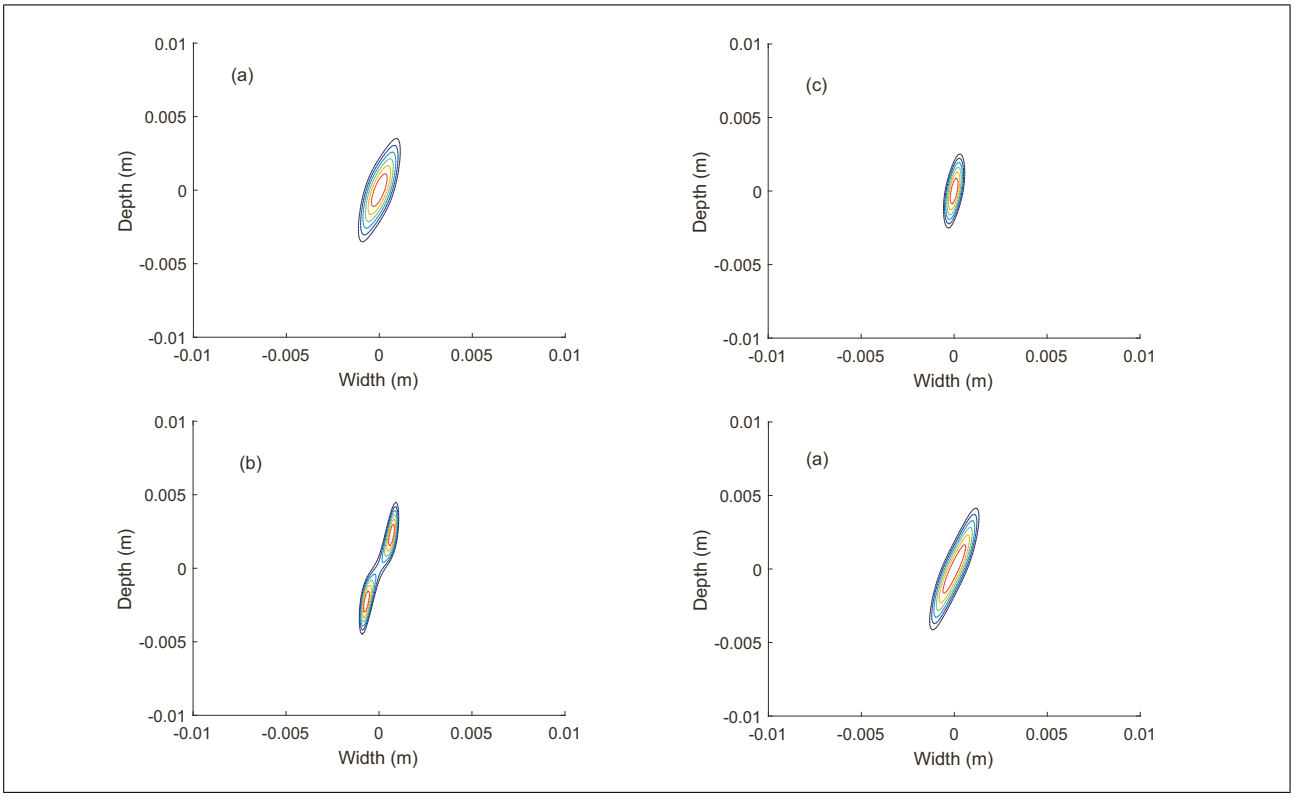

Figure 8. Crack reconstructions from FMC data arising from finite element simulation of the scattering of ultrasonic waves by a 5 mm crack with 40° orientation embedded in a heterogeneous medium by the Factorisation Method applied to (a) the scattering matrix arising at 1.5 MHz, (b) the scattering matrix arising at 1.5 MHz regularised by the TSVD ($m = 10$), (c) the multi-frequency scattering matrix and (d) the multi-frequency scattering matrix regularised by the TSVD ($m = 4$).

image (d) is obtained which better represents the nature of the tilted crack defect. However, at the −6 dB threshold, the diameter of the reconstructed flaw is 8 mm and its orientation is 69°, both presenting significant errors when compared to the known 5 mm length and 50° orientation.

A final simulated dataset where a 2.5 mm diameter disc was embedded in the parent material to the left of the weld was also interrogated. Here data arising from the central 64 elements of the 128 element linear array was used to generate the scattering matrices for inspection by the Factorisation Method, affording an angular aperture of 112°. The exact defect geometry is shown in Figure 9 (a). Image (b) shows the results from interrogation of the scattering matrix arising at 2.25 MHz whilst image (c) arises from the multi-frequency scattering matrix generated over the frequency range 1.125 MHz-3.375 MHz. In this case, taking the TSVD of the scattering matrix inhibited the method's ability to characterise the flaw. This can be attributed to the fact that the flaw is embedded in a homogeneous medium and since its scattering has been successfully isolated from that of the weld by limiting the aperture of inspection, taking the TSVD only serves to remove data relevant to the flaw. Additionally, the question of how many singular values should be considered can be avoided (although we have a suggested a thresholding technique in Section 2.2, how to optimally truncate the SVD remains an open question). The diameters of the disc (measured along the longest dimension) are 3.4 mm and 2.8 mm respectively. By using the multi-frequency scattering matrix, not only is the flaw size estimate improved but a lower aspect ratio ellipse is yielded and thus the disc nature of the defect is better defined.

To comment on the potential of the Factorisation Method as a tool for improved flaw characterisation, the standard time domain imaging algorithm, the Total Focussing Method (TFM) [2], has been applied to the datasets which gave rise to the reconstructions shown in Figures 8 and 9, and the results are plotted in Figure 10. On initial examination, it can be observed that the image of the crack in 10a better captures the 40° orientation of the defect. However, the −6 dB threshold gives rise to a crack length estimation of 9.8 mm, which compares poorly to the measurements obtained by each version of the Factorisation Method presented in Figure 8. Additionally, we observe two distinct peaks, a side effect which is inherent to the TFM imaging algorithm. This effect can also be observed (to a lesser extent) in plot 10 (b), which shows the reconstruction of the side-drilled hole embedded to the left of the austenitic weld. The reconstructed defect measures 6.7 mm along the horizontal, which compares poorly to the 2.8 mm measurement obtained using the multi-frequency factorisation method (recall the flaw has a diameter of 2.5 mm). Through further comparison of Figures 8, 9 and 10, it is also observed that the Factorisation Method better distinguishes between the crack defect and disc defect when the multi-frequency data are interrogated (images 8b

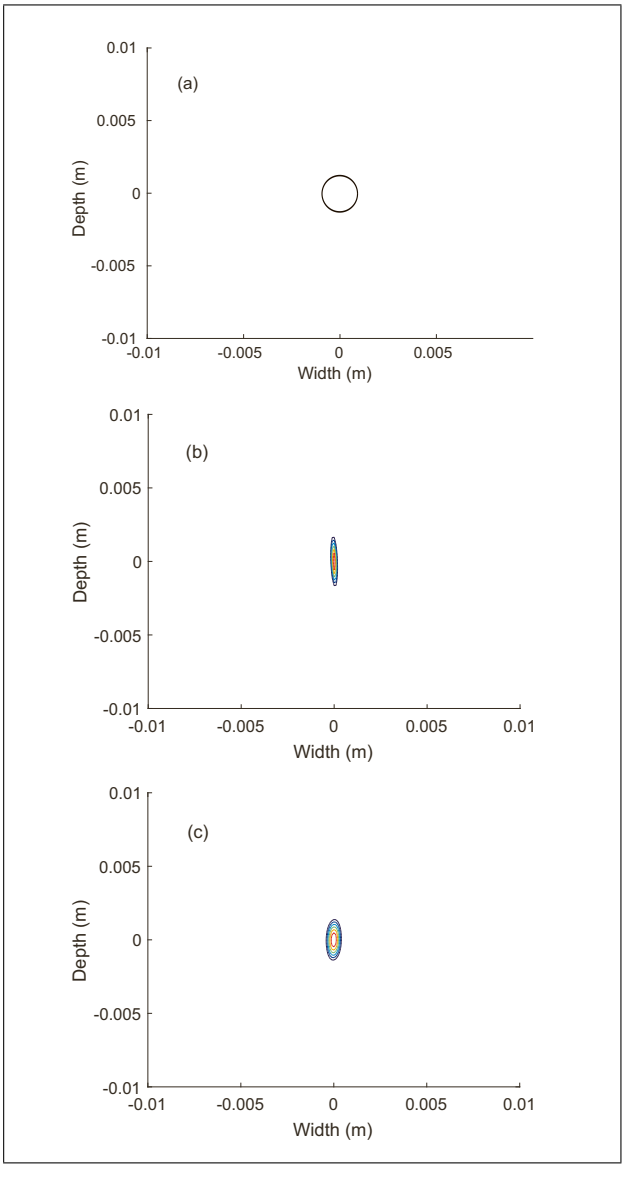

Figure 9. Reconstructions of a 2.5 mm diameter disc as shown in image (a) from FMC data arising from finite element simulation (see Table III) by the Factorisation Method applied to (b) the scattering matrix arising at 2.25 MHz and (c) the multi-frequency scattering matrix.

and 8d and 9c). This improved flaw identification complements previous work on flaw classification [38, 39] where the primary objective is to distinguish between crack defects and volumetric scatterers.

3.3. Application to Experimental FMC Data

Figure 11 depicts reconstructions of the 3 mm disc from the experimental data as detailed in Table III. Once again, the aperture had to be cropped to exclude interference of the flaw scattering by that of the back wall and so the scattering matrix used arises from the central 64 elements placed directly above the flaw (again affording an angular aperture of 112°). Image (a) shows the known defect size and geometry, image (b) arises from application of the factorisation method to the single frequency scattering matrix

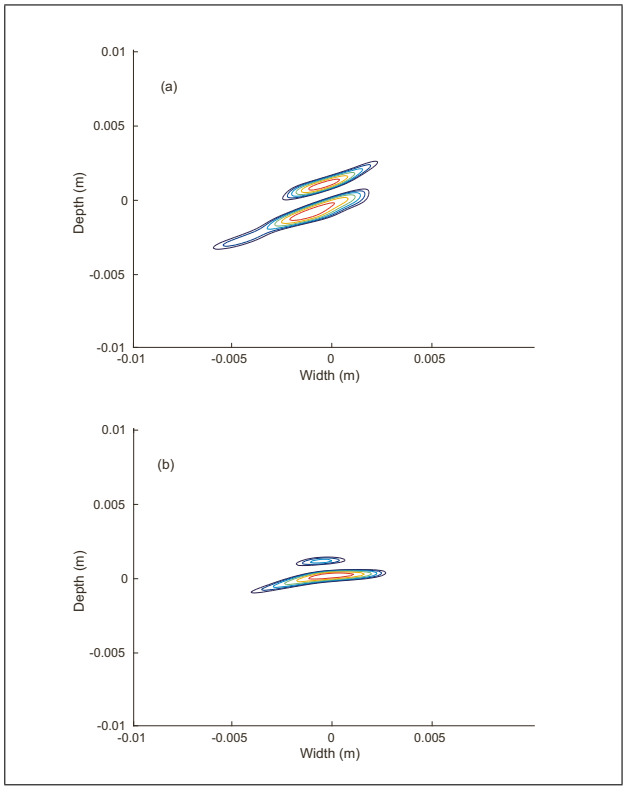

Figure 10. Reconstructions plotted at the −6 dB threshold of (a) the 5 mm crack embedded within the anisotropic steel weld and (b) the 2.5 mm diameter disc embedded to the left of the weld (see Tables I and II respectively) by the Total Focussing Method.

at 2.25 MHz and image (c) presents a similar reconstruction, this time arising from the multi-frequency scattering matrix generated by summing over the range 1.125 MHz–3.375 MHz at intervals equal to the sampling frequency, f_s. Note that the TSVD was not employed here as the flaw lies within the homogeneous parent material and so interference by the microstructue does not dominate the scattering matrix. Measuring the defects along their longest dimension gives rise to defect measurements of 4 mm and 2.9 mm respectively.

Figure 12 depicts reconstructions of the 7.8 mm crack from the experimental data as detailed in Table IV. Once again, the aperture had to be cropped to exclude interference of the flaw scattering by that of the back wall and so the scattering matrix used arises from the 42 elements placed directly above the flaw. This gives rise to an angular aperture of 122°. Note that due to the close proximity of the flaw to the backwall, it was not possible to entirely separate the scattering by the flaw from that of the backwall. Image (a) shows the known defect geometry and size. Image (b) arises from the single frequency scattering matrix at 5 MHz and image (c) arises from the multi-frequency scattering matrix generated by summing over the range 2.5 MHz–7.5 MHz at intervals equal to the sampling frequency, f_s. Measuring the defects along their longest dimension gives rise to defect measurements of 9.3 mm and 8.6 mm respectively, exhibiting relative errors of 19% in the case where the scattering matrix at a single

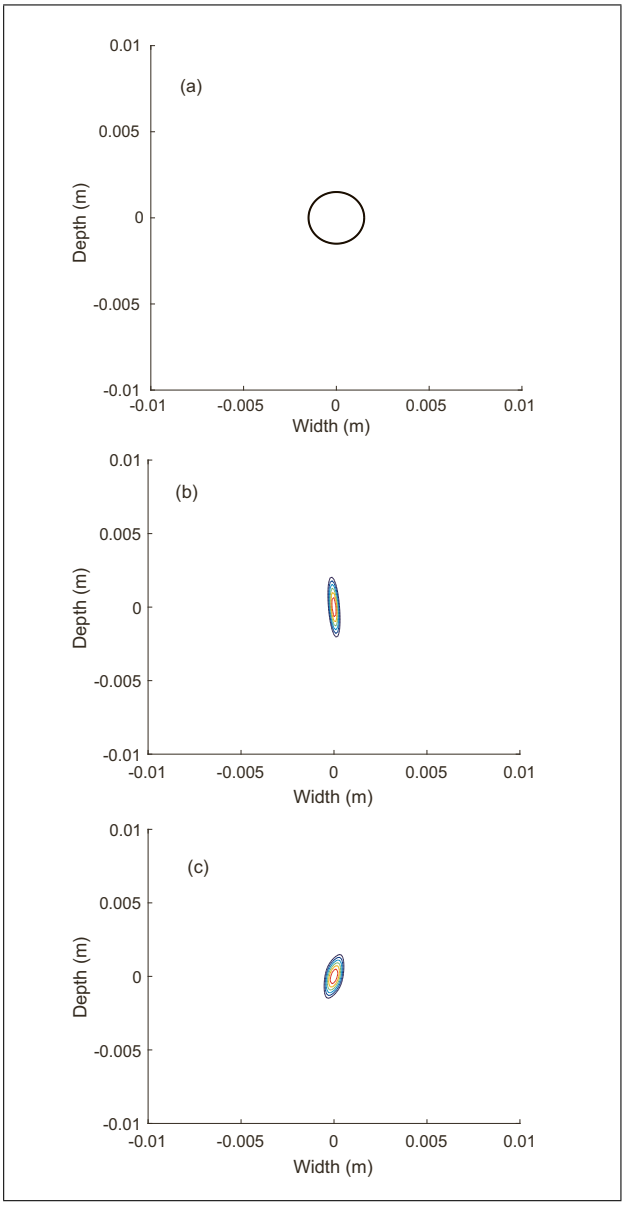

Figure 11. The geometry of the 3 mm diameter disc is plotted in (a). Reconstructions from FMC data arising from the phased array inspection of a steel block (see Table II) by the Factorisation Method applied to (b) the scattering matrix arising at 2.25 MHz and (b) the multi-frequency scattering matrix.

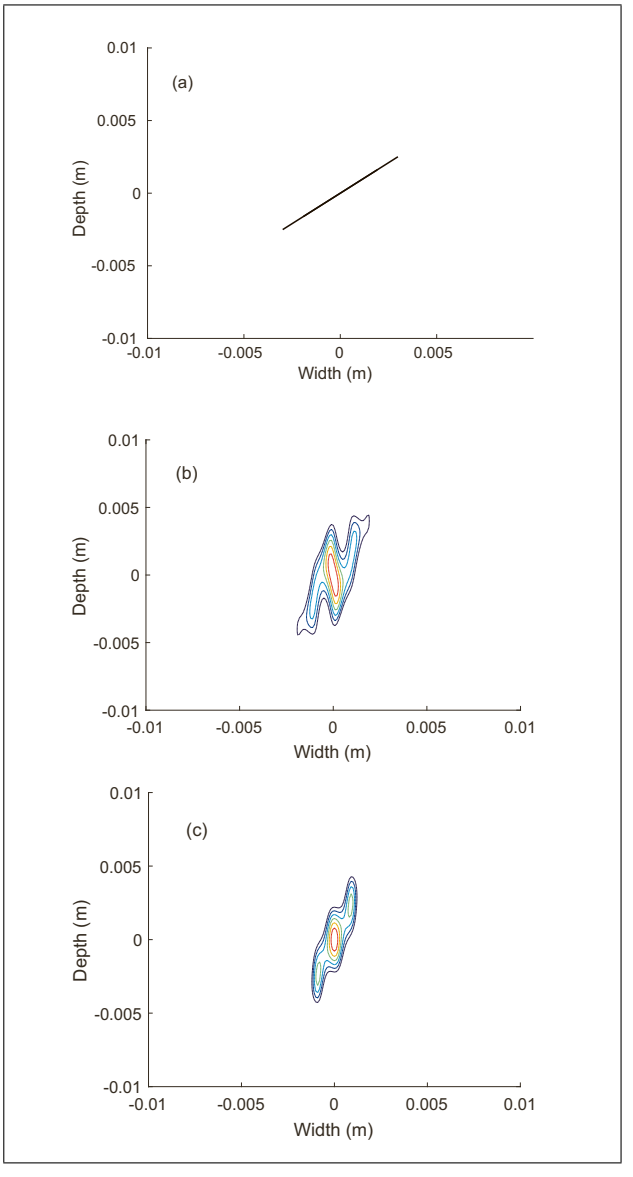

Figure 12. Reconstructions of the 7.8 mm crack orientated at 50° with respect to the x-axis shown in (a) from FMC data arising from the phased array inspection of welded austenitic plates (see Table IV) by the Factorisation Method applied to (b) the scattering matrix arising at 5 MHz and (c) the multi-frequency scattering matrix.

frequency is examined and an improved 10% error where multiple frequencies are considered. Furthermore, by using the multi-frequency scattering matrix, the defect can be better identified as crack like than from the image arising from the data at a single frequency: the ratio of the crack length to crack width (which should be large) is approximately 3.8 in the single frequency case, increasing to 5.2 in the multi-frequency case.

4. Conclusions

This paper has put forward a framework for using the Factorisation Method as a tool for flaw characterisation in the ultrasonic NDT industry. A brief derivation was provided to introduce the algorithm and subsequent application to synthetic time domain data as modelled in the software package PZFlex was carried out. Every case considered in this paper arose from limited aperture inspections with angles of inspection ranging between 83° and 122° (compared to the ideal 360° full aperture cases at which this method optimally performs). A method for isolating flaw scattering in the time domain before converting it to frequency domain scattering matrices was presented. Due to the time domain nature of the data, information was then made available for a range of frequencies at which scattering matrices could be generated and subsequently interrogated by the Factorisation Method. Initial implementation of the algorithm was carried out at the center frequency

of the transducer array before a multi-frequency approach was adopted. In the case where the flaw was embedded in highly scattering medium it was shown that by using only a subset of the singular values, interference by noise could be minimised. Additionally, the method outperformed the standard imaging algorithm (the total focussing method, TFM) in sizing and differentiating between two different types of flaws: a volumetric side-drilled hole and an angled crack-like scatterer. The algorithm was applied to two experimental data sets, one in which a side-drilled hole lay next to a weld and the other where a lack-of-fusion crack lay on the boundary of the weld. In both cases, taking the TSVD inhibited the Factorisation Method's performance (this can be attributed to the exclusion of valuable data). However, the multi-frequency approach yielded good flaw size estimates with errors of 0.1 mm for the 3 mm diameter side drilled hole and 0.7 mm for the 7.8 mm crack. And so, there remains much work to be done in order for the Factorisation Method to be adopted by end-users. However, this paper proposes a framework in which time domain, limited aperture data can be brought into the Factorisation Method domain. One natural direction to extend this work would be to consider the elastodynamic equations (rather than the Helmholtz equation). Also, it would be of interest to investigate the use of the Factorisation Method in the time-frequency domain [40].

Data Accessibility

The experimental data associated with this paper can be found at DOI:10.15129/60b6a5b8-e78e-4742-8414-aaba9399a9c8 and DOI:10.15129/086404bd-eb69-429b-978c-2c35cdbfcf87

Funding Statement

This work was funded through the UK Research Centre in NDE Targetted Programme by the Engineering and Physical Sciences Research Council (grant number EP/I019731/1) and latterly the iNEED project (grant number EP/P005268/1). Experimental samples were provided by Amec Foster Wheeler and Rolls Royce and software and support were supplied by Thornton-Tomasetti.

References

[1] B. W. Drinkwater, P.D. Wilcox: Ultrasonic Arrays for Non-destructive Evaluation: A Review. NDT & E Int **39** (2006) 525–541.

[2] C. Holmes, B. W. Drinkwater, P. D. Wilcox: Post Processing of the Full Matrix of Ultrasonic Transmit Receive Array Data for Non Destructive Evaluation. NDT & E Int **38** (2005) 701–711.

[3] P. D. Wilcox, C. Holmes, B. W. Drinkwater: Advanced Reflector Characterisation with Ultrasonic Phased Arrays in NDE Applications. IEEE TUFFC **54** (2007) 1541–1549.

[4] C. Li, D. Pain, B. W. Drinkwater, P. D. Wilcox: Imaging Composite Material Using Ultrasonic Arrays. NDT & E Int **53** (2013) 8–17.

[5] J. Zhang, B. W. Drinkwater, P. D. Wilcox, A. J. Hunter: Defect Detection Using Ultrasonic Arrays: The Multi-Mode Total Focusing Method. NDT & E Int, **43** (2009) 123–133.

[6] J. Zhang, B. W. Drinkwater, P. D. Wilcox: The use of Ultrasonic Arrays to Characterize Crack-like Defects. J. NDE **29** (2010) 222–232.

[7] J. Zhang, B. W. Drinkwater, P. D. Wilcox: Defect Characterization Using an Ultrasonic Array to Measure the Scattering Coefficient Matrix. IEEE TUFFC **55** (2008) 2254–2265.

[8] K. M. M. Tant, A. J. Mulholland, A. Gachagan: A Model-Based Approach to Crack Sizing With Ultrasonic Arrays. IEEE TUFFC **62** (2015) 915–926.

[9] L. Bai, A. Velichko, B. Drinkwater: Ultrasonic characterization of crack-like defects using scattering matrix similarity metrics. IEEE TUFFC **62** (2015) 545–559.

[10] A. Kirsch, N. Grinberg: The Factorisation Method for Inverse Problems. Oxford University Press, Oxford, 2008.

[11] A. Kirsch: Characterisation of the Shape of a Scattering Obstacle Using the Spectral Data of the Far Field Operator. Inverse Problems **14** (1998) 1489–1512.

[12] A. Kirsch: Factorization of the Far-Field Operator for the Inhomogenous Medium Case and an Application in Inverse Scattering Theory. Inverse Problems **15** (1999) 413–429.

[13] L. Bourgeois, E. Luneville: On the Use of Sampling Methods to Identify Cracks in Acoustic Waveguides. Inverse Problems **28** (2012) 105011.

[14] A. Kirsch: The MUSIC Algorithm and the Factorization Method in Inverse Scattering Theory for Inhomogenous Media. Inverse Problems **18** (2002) 1025–1040.

[15] C. Fan, M. Caleap, M. Pan, B. W. Drinkwater: A comparison between ultrasonic array beamforming and super resolution imaging algorithms for non-destructive evaluation. Ultrasonics **54** (2014) 1842–1850.

[16] D. Colton, A. Kirsch: A Simple Method for Solving Inverse Problems in the Resonance Region. Inverse Problems **12** (1996) 383–393.

[17] R. Potthast: A Survey on Sampling and Probe Methods for Inverse Problems. Inverse Problems **22**2 (2006).

[18] M. Ikehata: Reconstruction of the Shape of the Inclusion by Boundary Measurements. Co mm. PDEs **23** (1998) 1459–1474.

[19] R. Potthast: Stability Estimates and Reconstructions in Inverse Acoustic Scattering Using Singular Sources. J. Comput. Appl. Math **114** (2000) 247–274.

[20] V. Baronian, L. Bourgeois, A. Recoquillay: Imaging an acoustic waveguide from surface data in the time domain. Wave Motion **66** (2016) 68–87.

[21] Q. Chen, H. Haddar, A. Lechleiter, P. Monk: A sampling method for inverse scattering in the time domain. Inverse Problems **26** (2010) 085001.

[22] N. Khaji, S. H. D. Manshadi: Time domain linear sampling method for qualitative identification of buried cavities from elastodynamic over-determined boundary data. Computers & Structures **153** (2015) 36–48.

[23] C. D. Lines, S. N. Chandler-Wilde: A time domain point source method for inverse scattering by rough surfaces. Computing **75** (2005) 157–180.

[24] L. D. Russell, R. Potthast: The point source method for inverse scattering in the time domain. Mathematical methods in the applied sciences **29** (2006) 1501–1521.

[25] A. Kirsch, S. Ritter: A linear sampling method for inverse scattering from an open arc. Inverse problems **16** (2000) 89.

[26] F. Cakoni, D. Colton: The linear sampling method for cracks. Inverse problems **19** (2003) 279.

[27] Y. Boukari, H. Haddar: The Factorization method applied to cracks with impedance boundary conditions. Inverse Problems and Imaging.

[28] E. Kerbrat, C. Prada, D. Cassereau, M. Fink: Ultrasonic Nondestructive Testing of Scattering Media Using the Decomposition of the Time-Reversal Operator. IEEE TUFFC **49** (2002) 1103–1113.

[29] B. B. Guzina, F. Cakoni, C. Bellis: On the multi-frequency obstacle reconstruction via the linear sampling method. Inverse Problems **26** (2010) 125005.

[30] N. I. Grinberg: The Operator Factorization Method in Inverse Obstacle Scattering. IEOT **54** (2006) 333–348.

[31] Y. A. Abramovich, C. D. Aliprantis: An invitation to operator theory. Vol. 1. American Mathematical Soc., Rhode Island, USA, 2002.

[32] L. J. Cunningham, A. J. Mulholland, K. M. M. Tant, A. Gachagan, G. Harvey, C. Bird: The detection of flaws in austenitic welds using the decomposition of the time-reversal operator. Proc. R. Soc. A **472** No. 2188 (2016) 20150500.

[33] D. H. Chambers, A. K. Gautesen: Time reversal for a single spherical scatterer. JASA **109** (2001) 2616–2624.

[34] S. Shahjahan, F. Rupin, A. Aubry,, A. Derode: Evaluation of a multiple scattering filter to enhance defect detection in heterogeneous media. JASA **141** (2017) 624–640.

[35] PZFlex, Thornton Tomasetti Defence Ltd. 6th Floor South, 39 St Vincent Place, Glasgow, Scotland, G1 2ER, United Kingdom.

[36] G. Harvey, A. Tweedie, C. Carpentier, P. Reynolds: Finite Element Analysis of Ultrasonic Phased Array Inspections on Anisotropic Welds. AIP Conf. Proc. **1335** (2010) 827–834.

[37] I. Simonovski, L. Cizelj: Correlation length estimation in a polycrystalline material model. Proceedings of the International Conference Nuclear Energy for New Europe. Bled, Slovenia, Sept. 2005.

[38] M. Kitahara, K. Nakahata, S. Hirose: Elastodynamic inversion for shape reconstruction and type classification of flaws. Wave Motion **36** (2002) 443–455.

[39] S. Hirose: Inverse scattering for flaw type classification. Inverse Problems in Engineering Mechanics (1993) 359–366.

[40] K. M. M. Tant, A. J. Mulholland, M. Langer, A. Gachagan: A Fractional Fourier Transform Analysis of the Scattering of Ultrasonic Waves. PRSA **471** No.2175 (2015).